Journal of the Taiwan Institute of Chemical Engineers 178 (2026) 106396

Contents lists available at ScienceDirect

Journal of the Taiwan Institute of Chemical Engineers

journal homepage: www.journals.elsevier.com/journal-of-the-taiwan-institute-of-chemical-engineers

Self-precipitated metal-doped titanate nanofiber substrates for surface-enhanced Raman scattering of organic analytes

Yin-Hsuan Chang [a,1], Ming-Chung Wu [a,b,c,d,*,1], Ting-Han Lin [a,b], Jia-Mao Chang [a], Yu-Ching Huang [a,d,*], Jer-Chyi Wang [e,f,*]

[a] Department of Chemical and Materials Engineering, Chang Gung University, Taoyuan 333323, Taiwan
[b] Center for Sustainability and Energy Technologies, Chang Gung University, Taoyuan 333323, Taiwan
[c] Division of Neonatology, Department of Pediatrics, Chang Gung Memorial Hospital, Linkou, Taoyuan 333423, Taiwan
[d] Department of Materials Engineering, Ming Chi University of Technology, New Taipei City 243303, Taiwan
[e] Department of Electronic Engineering, Chang Gung University, Taoyuan 333323, Taiwan
[f] Department of Neurosurgery, Chang Gung Memorial Hospital, Linkou, Taoyuan 333423, Taiwan

ARTICLE INFO

Keywords:
Surface-enhanced Raman scattering
Hydrothermal synthesis
TiO_2
Photo-assisted Kelvin probe force microscopy
Pollutant detection

ABSTRACT

Background: Surface-enhanced Raman scattering (SERS) has emerged as a powerful technique for trace-level detection by leveraging localized surface plasmon resonance (LSPR) to amplify weak Raman signals. Although noble metal-modified TiO_2 shows great potential as a SERS substrate, conventional modification methods such as photodeposition and wet chemistry are often time-consuming, costly, and multi-step. We developed a straightforward hydrothermal synthesis to fabricate Au-doped titanate nanofibers with in-situ self-precipitated Au nanoparticles to overcome these limitations. This method offers a scalable and efficient platform for enhancing SERS performance broadly applicable to environmental and industrial pollutant monitoring.

Methods: Various titanate nanofibers with different incorporated metal ions were synthesized via a hydrothermal method. Self-precipitated Au nanoparticles are uniformly integrated onto sodium titanate fibers to enhance surface plasmon resonance behavior. Comprehensive characterization, including synchrotron X-ray diffraction, XPS, UV–Vis, Raman spectroscopy, and photo-assisted Kelvin probe force microscopy (photo-KPFM) are employed to confirm successful nanoparticle integration and assess plasmonic enhancement.

Significant findings: The Au doped titanate substrate demonstrates superior SERS performance, achieving an analytical enhancement factor (AEF) of 185,000 for methylene blue detection at concentrations as low as 3.0×10^{-9} g/cm^2. The findings establish Au-doped titanate nanofibers as a scalable, sensitive platform for organic pollutant detection with potential applications in environmental monitoring and analytical sensing.

1. Introduction

Traditional analytical techniques such as high-performance liquid chromatography (HPLC) and gas chromatography-mass spectrometry (GC–MS) are widely employed for chemical detection. Although these methods offer exceptional sensitivity and precision, they come with drawbacks such as lengthy sample preparation and costly instrumentation, which limit their practicality for on-site, real-time monitoring [1, 2]. Surface-enhanced Raman scattering (SERS) has emerged as a powerful ultrasensitive technique for the trace detection of molecules [3–6]. By utilizing metallic nanostructures, SERS significantly amplifies weak Raman signals while maintaining the non-destructive properties of conventional Raman spectroscopy. This signal enhancement stems from localized surface plasmon resonance (LSPR) and interactions between the analyte and substrate, enabling the detection of trace amounts of molecules with high specificity [7–10]. Compared to conventional methods, SERS platform provides several advantages, including low cost, rapid detection, minimal sample preparation, and real-time monitoring capabilities, making it a valuable tool for environmental and industrial applications.

TiO_2 exists in various crystalline and amorphous forms and has been extensively studied as a multifunctional material, including SERS

---

* Corresponding authors.

E-mail addresses: mingchungwu@cgu.edu.tw (M.-C. Wu), huangyc@mail.mcut.edu.tw (Y.-C. Huang), jcwang@mail.cgu.edu.tw (J.-C. Wang).

[1] These authors contributed equally to this work.

https://doi.org/10.1016/j.jtice.2025.106396
Received 16 April 2025; Received in revised form 4 September 2025; Accepted 7 September 2025

application [9–17]. The detection and monitoring of pollutant are of significant interest in environmental science, food safety, and wastewater treatment due to their widespread use and potential toxicity. Li et al. realized PS nanoplastics SERS detection through honeycomb Ag@TiO_2 substrate-based SERS. The LSPR of the plasmonic AgNPs and the charge transfer between Ag and TiO_2 significantly enhance the electromagnetic field and boost the overall performance [15]. Huang et al. demonstrated Ag@TiO_2@cotton substrates with good SERS sensitivity for methylene blue. An obvious improved EM field was found in the nanocavities on the surface of the prepared porous TiO_2 layer [14]. TiO_2 modified with noble metal nanoparticles as a SERS substrate and its enhancement mechanisms have been widely reported. However, conventional modification techniques such as photodeposition [18,19], wet chemistry, and chemical vapor deposition are often costly and involve multiple steps. Lin et al. proposed a facile one-pot hydrothermal synthesis strategy to overcome the limitations of traditional multi-step and high-cost modification methods. This approach enables the in-situ formation of Ag-doped TiO_2 nanofibers, followed by calcination that induces the surface precipitation of Ag nanoparticles [20].

In this study, we developed a simple and effective method for fabricating surface-enhanced Raman scattering substrates by self-assembling uniformly dispersed metal nanoparticles onto a titanate nanofiber matrix via a hydrothermal method. The resulting nanofiber was designed to function as a fixed-position sensing platform, allowing analyte solutions to be directly applied without extensive sample pretreatment. The interconnected fibrous network not only provides a high surface area for molecular adsorption but also facilitates optical penetration due to its porous structure. As a result, laser excitation can efficiently reach analyte molecules distributed throughout the depth of the substrate, while scattered Raman signals are effectively collected. The photo-induced surface potential behavior of Au-doped titanate fibers using photo-KPFM was measured to uncover the fundamental light-matter interactions. For the SERS application, 4 different organic dyes, including methyl red (MR), methyl orange (MO), brilliant green (BG), and methylene blue (MB), are selected as the tested specimen. A remarkable enhancement of 185,000-fold enhancement has been observed for MB on the Au doped titanate SERS substrate. This technique offers high sensitivity, low cost, and rapid response, making it suitable for the detection of organic compounds and environmental pollutant.

2. Experimental method

2.1. Synthesis of metal-doped TiO_2 nanofibers

5.0 mol % metal-doped TiO_2 nanofibers were synthesized using the hydrothermal method. 2.50 g anatase TiO_2 powder (98 %, ACROS) and metal precursor, including, platinum (II) acetylacetonate ($C_{10}H_{14}O_4Pt$, 98 %, ACROS), copper (II) nitrate trihydrate ($Cu(NO_3)_2 \cdot 3H_2O$, 99 %, ACROS), silver nitrate ($AgNO_3$, 99 %, CHONEYE), and tetrachloroauric (III) acid trihydrate ($HAuCl_4 \cdot 3H_2O$, ACROS), were suspended in 62.5 mL 10 M NaOH aqueous solution (>97 %, Fisher Scientific). The reactants were transferred into a Teflon-lined autoclave and vigorously agitated and stirred for 30 min. Subsequently, the mixture solution underwent thermal treatment at 150 °C for 24 h. Various transition metal-doped sodium titanate ($Na_2Ti_3O_7$), washed with deionized water until neutralized, were obtained and denoted as M-$Na_2Ti_3O_7$ (M = Pt, Cu, Ag, Au). Subsequently, 0.10 M HCl (37 %, ACROS) was used to exchange the sodium ions for protons, followed by further washing with deionized water until neutralized. The resulting Au-doped hydrogen titanate ($H_2Ti_3O_7$) was then filtered and dried in air at 80 °C, denoted as M-$H_2Ti_3O_7$. Finally, M-$H_2Ti_3O_7$ was calcined under air atmosphere and H_2/N_2 atmosphere at 600 °C for 12 h with an ascending rate of 5 °C/min. The samples were named M-TiO_2-air and M-TiO_2-H_2, respectively.

2.2. Material characterization

The morphology was investigated by field-emission scanning electron microscope (FESEM, SU8010, Hitachi, Japan) and spherical aberration corrected field-emission transmission electron microscope (FETEM, JEM-ARM200FTH, JEOL, Japan). The X-ray spectra were performed by synchrotron X-ray spectroscopy ($\lambda \sim 1.025$ Å) on beamline 13A1 of the National Synchrotron Radiation Research Center (NSRRC) in Taiwan and recorded from 2θ between 5° to 45° with a 0.01° step at 0.02° s^{-1}. The UV–VIS absorption spectra were recorded by the UV–VIS spectrophotometer (1900i, Shimazu, Japan) with a scan rate of 400 $nm \cdot min^{-1}$ and a data interval of 1.0 nm. The surface potential evaluation with and without light irradiation was measured using an ambient scanning Kelvin probe system (SKP5050, KP technology, United Kingdom). The Raman spectra were obtained by Raman spectroscopy (UniRAM, CL Technology Co., Ltd, Taiwan). For the evaluation of SERS performance, each spectrum was obtained by averaging 20 individual signal acquisitions, which were merged by the measurement system into a single representative spectrum. This procedure effectively improves the signal-to-noise ratio and minimizes random fluctuations, thereby ensuring the reproducibility and reliability of the collected spectra. The adsorption behavior of various Au-doped nanofiber SERS substrates was investigated by dispersing 20 mg of each Au-doped nanofiber SERS substrate in a 10 ppm methylene blue aqueous solution. The adsorption performance was assessed by measuring the concentration of methylene blue at different time points and calculating the ratio of $\boldsymbol{C_t/C_0}$, where $\boldsymbol{C_0}$ is the initial methylene blue concentration, $\boldsymbol{C_t}$ is the methylene blue concentration at various times. X-ray Photoelectron spectrometer with an X-ray source of Al Kα (K-alpha X-ray photoelectron spectrometer, Thermo Fisher Scientific, USA) was used to analyze the chemical state.

2.3. Results and discussion

Fig. 1(a) presents a proposed schematic illustrating the structural evolution of metal doped titanate nanofibers during proton exchange via acid washing and subsequent heat treatment. Initially, commercial anatase TiO_2 particles were dissolved in 10.0 M NaOH, where highly reactive hydroxide ions attacked the Ti-O-Ti bonds, leading to the formation of octahedral $Ti(OH)_6^{2-}$ units. During hydrothermal treatment, these units are assembled to form sodium titanate nanostructures. To modify the composition, an acid-washing step with diluted HCl was employed to exchange Na^+ ions with H^+ ions, resulting in the formation of hydrogen titanate. Finally, the hydrogen titanate underwent a calcination process under different atmospheres: in air to produce highly crystalline TiO_2, or in a H_2/N_2 atmosphere to introduce oxygen vacancies and Ti^{3+} defects. Fabrication of the SERS substrate is illustrated in Fig. 1 (b). The washers are attached to glass slides using copper tape. Subsequently, the as-prepared specimens were filled into the hollow cavities of washers to obtain a fixed-position sensing platform. The interconnected fibrous network not only provides a high surface area for molecular adsorption but also facilitates optical penetration due to its porous structure. A specific volume of dye solutions, including methyl red ($C_{15}H_{15}N_3O_2$), methyl orange (($C_6H_4(OH)_2$), brilliant green ($C_{27}H_{34}N_2O_4S$), and methylene blue ($C_{16}H_{18}N_3SCl$), were dropped onto the SERS substrates. The substrates were dried overnight and stored in an inert environment for future use.

Fig. 2 presents a series of metal doped sodium titanate (M-$Na_2Ti_3O_7$, M = Pt, Cu, Ag, Au) synthesized with 5.0 mol % doping concentration. The morphological analysis in Fig. 2(a-d) reveals the distinct characteristics of each doped variant: (a) Pt-$Na_2Ti_3O_7$, (b) Cu-$Na_2Ti_3O_7$, (c) Ag-$Na_2Ti_3O_7$, and (d) Au-$Na_2Ti_3O_7$. All M-$Na_2Ti_3O_7$ exhibit an ultralong and belt-like morphology with lengths extending up to several hundred micrometers. Notably, Au-$Na_2Ti_3O_7$ and Pt-$Na_2Ti_3O_7$ display metallic nanoparticles dispersed on the sodium titanate surface, as further confirmed by XRD and UV–Vis spectroscopy. The synchrotron X-ray patterns (Fig. 2(e)) show the characteristic diffraction peaks at 2θ =

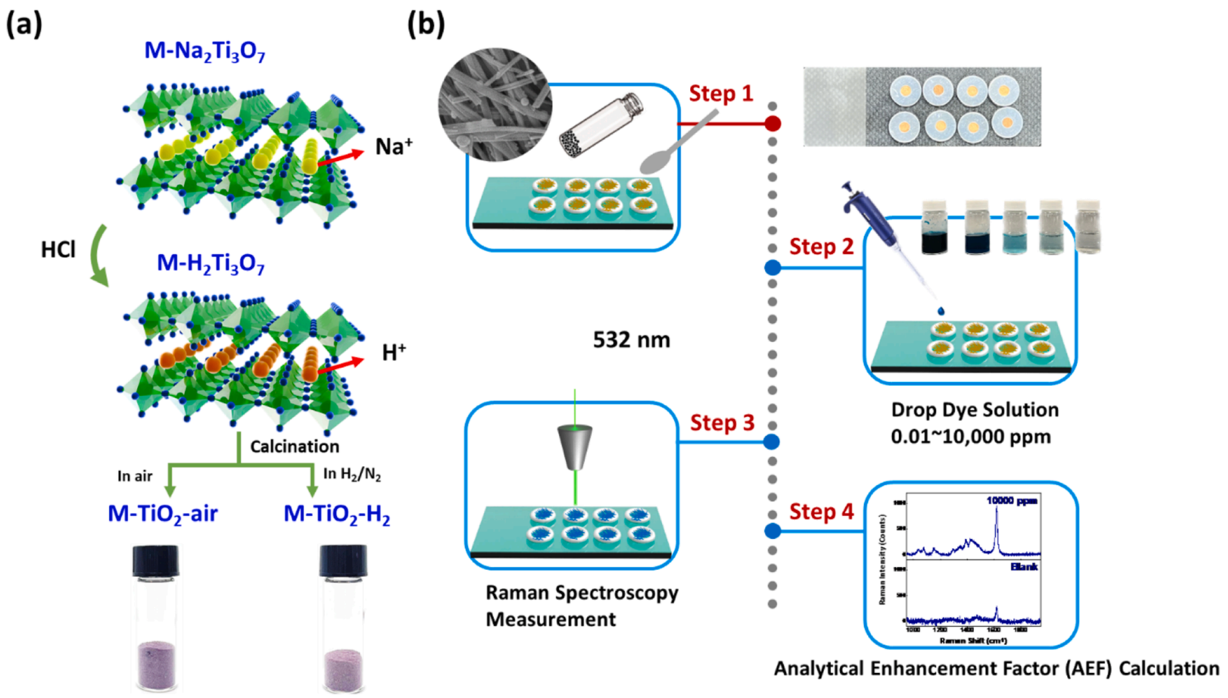

Fig. 1. **(a)** Schematic of the formation of titanate nanofibre by hydrothermal synthesis. **(b)** Illustration of the SERS substrate fabrication.

7.1°, 16.6°, 19.8°, 22.7°, and 31.8 °corresponding to the (001), (201), (111), ($\bar{1}$12), and (401) planes of sodium titanate. The low-intensity reflections indicate a highly disordered crystalline structure, suggesting that sodium ion incorporation induces a phase transition with significant lattice distortion. Additionally, Au-$Na_2Ti_3O_7$ and Pt-$Na_2Ti_3O_7$ exhibit strong metallic signals, indicating successful metal precipitation on the surface. The high concentration of metallic species is expected to modify the physicochemical properties of sodium titanate, particularly through surface plasmon resonance, which is highly dependent on the dispersion and electronic interactions of the embedded metal nanoparticles. The normalized UV–Vis absorbance spectra (Fig. 2(f)) compare the optical properties of M-$Na_2Ti_3O_7$, and the color transformation associated with these doping elements is shown in Fig. 2(g). The UV–Vis absorbance spectra highlight the plasmonic resonance effects induced by metal doping. Notably, Pt-$Na_2Ti_3O_7$ and Au-$Na_2Ti_3O_7$ exhibit a pronounced absorbance enhancement within the 400–800 nm wavelength range, which can be attributed to the surface plasmon resonance of Pt and Au nanoparticles precipitated on the sodium titanate surface. The corresponding XPS spectra (**Figure S1**) further confirm the oxidation states of the incorporated elements. Specifically, Au-$Na_2Ti_3O_7$ and Pt-$Na_2Ti_3O_7$ exhibit distinct metallic signals in the Au *4f* and Pt *4f* regions, respectively. In contrast, the Cu-$Na_2Ti_3O_7$ sample displays features characteristic of Cu_2O, while the Ag-$Na_2Ti_3O_7$ sample shows signals corresponding to Ag_2O. These findings are consistent with the UV–Vis absorbance trends, indicating the presence or absence of plasmonic effects depending on the metal oxidation state.

In order to investigate the photoresponse of our fabricated sample under light sources, we employed photo-assisted Kelvin probe force microscopy (photo-KPFM) to examine the spatial charge separation under UV LED irradiation at a wavelength of 365 nm (Fig. 2(h-k)). All materials are plated and examined onto a gold substrate for the photo-KPFM measurement. KPFM is a powerful technique for measuring the work function of semiconductor materials and studying charge carrier transfer under both dark and illuminated conditions. The contact potential difference (CPD) is the difference in work function (Φ) between sample and tip. Since the tip's work function is constant, the measured CPD is directly related to the sample's Fermi level. The change of the CPD is shown in Eq. (1):

$$\Delta CPD = CPD_{illumination} - CPD_{dark} \quad (1)$$

The CPD value is determined by the concentration of charge carriers present at the sample surface. Upon illumination, photogenerated electrons migrating to the surface raise the Fermi level of the sample, resulting in a decrease in its work function and a corresponding increase in the CPD [21–25]. The effect of UV light irradiation on the CPD changes of various M-$Na_2Ti_3O_7$ was investigated. The ΔCPD of each specimen under UV irradiation is summarized in Table 1. The CPD of Au-$Na_2Ti_3O_7$ (−8.9 mV) and Pt-$Na_2Ti_3O_7$ (−5.9 mV) showed a prominent decrease after irradiation compared with Cu-$Na_2Ti_3O_7$ and Ag-$Na_2Ti_3O_7$. This can be attributed to the presence of metallic Au and Pt nanoparticles on the surface, which can prevent the photogenerated electron be trapped in the trap state of poor crystalline sodium titanate. Upon UV irradiation, electrons gain sufficient energy to overcome the Schottky barrier and transfer to the surface-deposited metal nanoparticles, resulting in an increased electron accumulation at the surface. In contrast, the positive ΔCPD observed for Ag-$Na_2Ti_3O_7$ may be attributed to the presence of oxidized silver species, such as Ag_2O, rather than metallic Ag^0. These oxidized species limit their ability to trap or accumulate photogenerated electrons. The above analysis confirms the formation of metallic nanoparticles on the surface, which is advantageous for subsequent SERS applications.

Given the superior material properties of Au-$Na_2Ti_3O_7$, further synthesis was carried out to explore and expand its potential applications. The microstructure of Au-$Na_2Ti_3O_7$ was investigated by TEM (**Figure S2** and **S3**), which provided insights into the distribution of Au NPs within the sodium titanate nanofibers. The low-magnification TEM image reveals a uniform distribution of Au nanoparticles across the sodium titanate nanofiber network without noticeable aggregation. The high-resolution TEM images (**Figure S2(d-f)**) further confirm the intimate interface between the nanoparticles and the nanofiber matrix, supporting that the Au nanoparticles are effectively attached rather than mixed with nanofibers. Besides, the particles size of Au is ~ 60 nm. To further examine the elemental distribution, EDS elemental mapping images were obtained. The Ti, O, and Na signals exhibited a homogeneous distribution throughout the region of the sodium titanate template. The Au signals were primarily concentrated in the outer region of

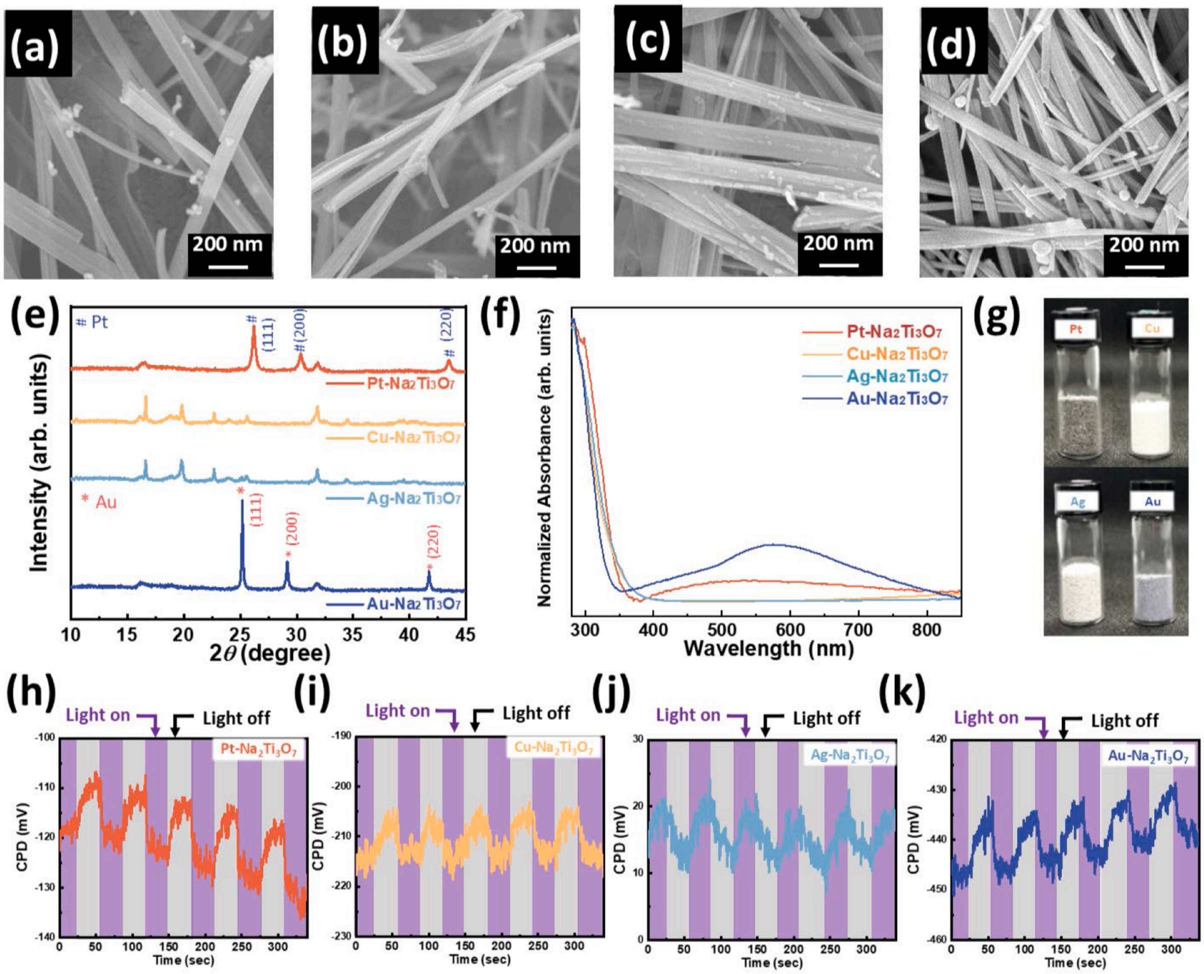

Fig. 2. SEM images of **(a)** Pt-$Na_2Ti_3O_7$, **(b)** Cu-$Na_2Ti_3O_7$, **(c)** Ag-$Na_2Ti_3O_7$, and **(d)** Au-$Na_2Ti_3O_7$. **(e)** synchrotron X-ray diffraction patterns, **(f)** UV–Vis absorption spectra, and **(g)** digital photo of various M-$Na_2Ti_3O_7$. Contact potential differences with light-on/off cycles under UV LED (365 nm): **(h)** Pt-$Na_2Ti_3O_7$, **(i)** Cu-$Na_2Ti_3O_7$, **(j)** Ag-$Na_2Ti_3O_7$, and **(k)** Au-$Na_2Ti_3O_7$.

Table 1
Contact potential differences of various M-$Na_2Ti_3O_7$ under UV LED illumination.

Sample	ΔCPD (mV)
Pt-$Na_2Ti_3O_7$	−7.3
Cu-$Na_2Ti_3O_7$	−5.9
Ag-$Na_2Ti_3O_7$	3.6
Au-$Na_2Ti_3O_7$	−8.9

the particles.

Fig. 3 demonstrates a systematic study of Au-$Na_2Ti_3O_7$, Au-$H_2Ti_3O_7$, Au-TiO_2-air, and Au-TiO_2-H_2. Fig. 3(a) shows the synchrotron X-ray pattern of various Au-doped nanofibers. The Au-$Na_2Ti_3O_7$ shows the characteristic diffraction peaks corresponding to sodium titanate [26]. The insignificant crystallized structure of sodium titanate implied that sodium ion leads to the phase transition with a high degree of disorder. After the calcination process, the poor crystallized structure of Au-$H_2Ti_3O_7$ was totally transformed into anatase TiO_2. Hydrogen titanate is transformed to anatase phase when the calcination temperature is set at 600 °C. The diffraction peaks at 2θ of 16.8°, 31.5°, 35.1°, and 35.9° correspond to the (101), (200), (105), and (211) planes of anatase phase TiO_2. All the specimens show strong metallic signals. Considering the overlapping characteristic peaks of Au (111) plane and (103), (004), and (112) planes of anatase TiO_2, Au (200) plane was selected to calculate the crystallite size by the Scherrer equation. The calculated crystallite sizes are ~35.7 nm (Au-$Na_2Ti_3O_7$), ~42.4 nm (Au-$H_2Ti_3O_7$), ~56.5 nm (Au-TiO_2-air), and ~56.5 nm (Au-TiO_2-H_2). **Figure S4** shows the synchrotron X-ray pattern of various M-doped nanofibers. The diffraction peaks confirm that both Au- and Pt-doped nanofibers retain their metallic phases, indicating that no significant oxidation occurred during the synthesis process. For the Ag-doped samples, metallic Ag was not prominently observed in the as-prepared $Na_2Ti_3O_7$ structure. After HCl washing, the Ag species predominantly converted to AgCl. Upon subsequent air calcination, AgCl was further oxidized to form Ag_2O. In contrast, calcination under a hydrogen atmosphere resulted in the reduction of Ag species, restoring the metallic Ag phase. No distinct crystalline phase related to Cu was observed in the XRD patterns.

From the Raman spectra (Fig. 3(b)), the Raman band appearing at 282, 447, 660, and 913 cm^{-1} are indicative of the characteristic stretching modes of sodium titanate. The peak at 159 and 191 cm^{-1} can be ascribed to lattice modes of Na^+-O-Ti. The Raman peaks at 282, 447, and 660 cm^{-1} are corresponding to the Ti-O-Ti stretching modes. The Raman peaks at 913 cm^{-1} are the Ti-O stretching involving non-bridging oxygen atoms [27,28]. For the anatase phase of TiO_2, the major Raman bands are located at 148, 197, 397, 511, and 638 cm^{-1}, with superimposed Raman bands at ~515 cm^{-1}. The individual Raman bands are attributed to the six Raman-active modes of anatase TiO_2 phase with the symmetries of E_g, E_g, B_{1g}, A_{1g}, B_{1g}, *and* E_g. Raman shift of various organic compounds usually present at large Raman shift region, being higher than 1000 cm^{-1}. From the inset of Fig. 3(b), there is no obvious Raman shift being higher than 1000 cm^{-1}. This is advantageous for SERS

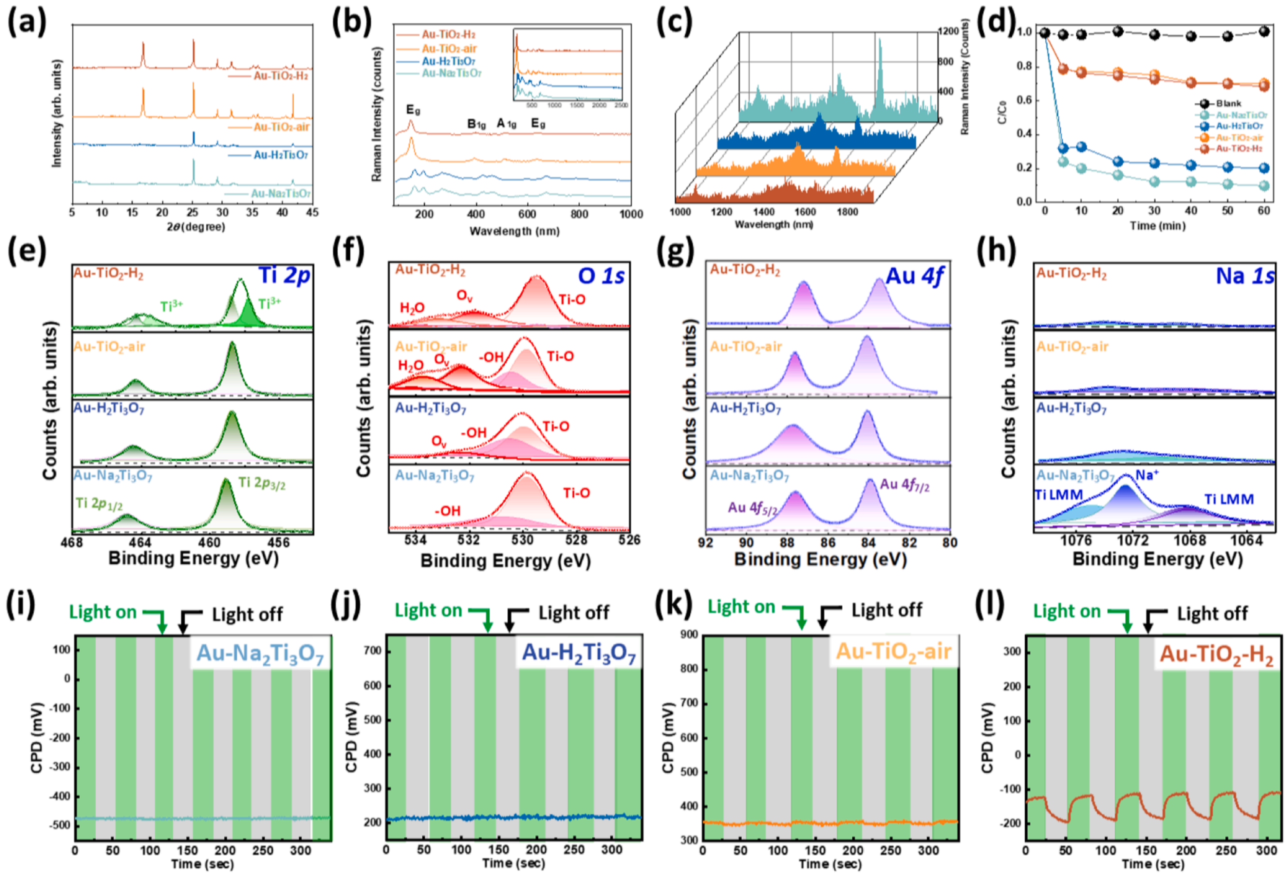

Fig. 3. **(a)** Synchrotron X-ray diffraction patterns and **(b)** Raman spectra of Au-$Na_2Ti_3O_7$, Au-$H_2Ti_3O_7$, Au-TiO_2-air, and Au-TiO_2-H_2. **(c)** Raman spectra and **(d)** adsorption behavior of methylene blue on various SERS substrates. XPS spectra for **(e)** Ti ***2p*** orbital, **(f)** O ***1s*** orbital, **(g)** Au ***4f*** orbital, and **(h)** Na ***1s*** orbital. Contact potential differences with light-on/off cycles under green LED (530 nm): **(i)** Au-$Na_2Ti_3O_7$, **(j)** Au-$H_2Ti_3O_7$, **(k)** Au-TiO_2-air, **(l)** Au-TiO_2-H_2.

sensing applications, as it allows the detection of analytes without interference from substrate signals. Fig. 3(c) shows the Raman spectra of 3.0×10^{-8} g/cm^2 methylene blue on various Au-doped nanofiber SERS substrates. We hypothesize that a closer match between the absorption wavelength of the dye and the excitation wavelength of the Nd:YAG green laser ($\lambda = 532.8$ nm) will lead to a more pronounced enhancement of the Raman signals. This hypothesis suggests that when the absorption wavelength of the dye is in proximity to the laser excitation wavelength, there will be a stronger amplification of the Raman scattering, resulting in more prominent Raman signal enhancement. Based on this, methylene blue was selected as the target analyte for our study. The concentrations of methylene blue measured using various Au-doped nanofiber SERS substrates are fixed in 3.0×10^{-8} g/cm^2. The high intensity of Au-$Na_2Ti_3O_7$ nanofiber SERS substrate is speculated to be the high adsorption of sodium titanate (Fig. 3(d)). The presence of sodium titanate is known to promote a higher density of analyte molecules adsorbed on Au-$Na_2Ti_3O_7$ nanofiber SERS substrates, leading to a more pronounced Raman signal enhancement.

To comprehensively investigate the electronic states and chemical composition of various Au-doped titanate nanofibers, XPS was conducted to analyze the electronic configuration of such elements (Fig. 3 (e-h)). The Ti ***2p*** peaks at 459.0 and 464.7 eV are assigned to Ti $\boldsymbol{2p_{3/2}}$ and Ti $\boldsymbol{2p_{1/2}}$, respectively. Compared with that of Au-$Na_2Ti_3O_7$, the binding energy of Au-TiO_2-air, and Au-TiO_2-H_2 is shifted toward lower binding energy. Two additional peaks corresponding to Ti^{3+} $\boldsymbol{2p_{3/2}}$ and Ti^{3+} $\boldsymbol{2p_{1/2}}$ states appear in Au-TiO_2-H_2. These observations indicate the introduction of Ti^{3+} interstitial defects after the calcination process carried out under H_2/N_2 atmosphere. For the O ***1s*** spectra, the fitted peaks at ~530.5 can be referred to Ti-O bonds in TiO_2 crystal lattices. In general, the peak at 531.5 eV is ascribed to the surface hydroxyl (OH^-). The XPS results for Au-TiO_2-H_2 suggest that the crystal surface has oxygen vacancy defects and Ti^{3+} interstitial defects. For the Na ***1s*** spectra, the signals are affected by the presence of the titanium due to their overlapping with Ti LMM. The comparison shows that after acid wash, there is no Na ***1s*** signal, indicating that Na^+ has been removed completely.

Under green LED illumination (530 nm), the ΔCPD of Au-doped samples is undetectable for Au-$Na_2Ti_3O_7$ and Au-$H_2Ti_3O_7$, and is 6.8 and 69.2 mV for Au-TiO_2-air and Au-TiO_2-H_2, respectively. (Fig. 3(i-l)). The undetectable ΔCPD suggests that the energy from the green laser fails to induce electron-hole separation and is likely entirely converted to reflection and scattering. Furthermore, the reflectance of Au-doped samples, as evident from the absorption spectra (**Figure S5**), is not significantly high, suggesting that the Au-doped titanate fibers materials are a potential candidate for SERS substrates due to their pronounced scattering behavior.

Table 2

For the SERS application, 4 different organic dyes, including methyl red (MR), methyl orange (MO), brilliant green (BG), and methylene blue

Table 2
Contact potential differences of various Au-doped nanofiber under green LED irradiation.

Sample	ΔCPD (mV)
Au-$Na_2Ti_3O_7$	0.0
Au-$H_2Ti_3O_7$	0.0
Au-TiO_2-air	6.9
Au-TiO_2-H_2	69.2

(MB), are selected as the tested specimen. The chemical structure of each organic dye is shown in Fig. 4(a-d). These toxic organic dyes persist in aquatic ecosystems, reducing light penetration and oxygen solubility, disrupting photosynthesis, and posing carcinogenic and mutagenic risks to aquatic life, plants, and human health. For UV–Vis spectra (Fig. 4(e)), the λ_{max} for methyl red, methyl orange, brilliant green, and methylene blue are 429, 463, 625, and 664 nm, respectively. The λ_{max} of PL spectra for methyl red, methyl orange, brilliant green, and methylene blue are 512, 557, 664, and 698 nm, respectively. It is commonly observed that the PL peak occurs at higher energy (30–100 nm) compared to the absorption peak. By comparing the results obtained from absorption spectra and PL spectra, the Stokes shifts were observed. The Raman analysis for four kinds of organic dyes are shown in Fig. 4(f). The respective band wavenumbers and their corresponding assignments for these dyes are provided in **Table S1**. It is noteworthy that all the Raman signals appear at Raman shift higher than 1000 cm^{-1}. This is advantageous as it ensures that the Raman signals of the organic dyes will not overlap with the Raman signals of our fabricated SERS substrates, simplifying the process of distinguishing and analyzing their respective Raman spectra. This characteristic facilitates the accurate and reliable detection and identification of organic dyes using SERS techniques.

The versatility of the Au-$Na_2Ti_3O_7$ substrate was explored by investigating its performance in detecting methyl red, methyl orange, brilliant green, and methylene blue (Fig. 5). To determine the detection capabilities of Au-$Na_2Ti_3O_7$ for each dye, specific Raman shifts were identified and utilized for the calculation of the analytical enhancement factor (***AEF***). ***AEF*** can be applied to analytes, which are first present in solution or gas phase, and then are deposited/adsorbed onto the SERS substrate (either solid or colloidal) [29,30]. The SERS enhancement is quantified by estimating the ***AEF*** as shown below:

$$\boldsymbol{AEF} = \frac{\boldsymbol{I_{SERS}}}{\boldsymbol{I_{Raman}}} \times \frac{\boldsymbol{C_{Raman}}}{\boldsymbol{C_{SERS}}} \tag{2}$$

Where $\boldsymbol{I_{SERS}}$ and $\boldsymbol{I_{Raman}}$ are the signal intensities recorded using SERS and normal Raman at their respective concentrations. $\boldsymbol{C_{SERS}}$ and $\boldsymbol{C_{Raman}}$ are the concentrations of dye measured using various nanofiber SERS substrates and normal Raman.

For the detection of methyl red, the Raman shift at 1396 cm^{-1}, which corresponds to the $N = N$ stretching band, was selected for ***AEF*** calculation [31]. Similarly, for methyl orange detection, the Raman shift at 1420 cm^{-1}, also associated with the $N = N$ stretching band, was employed [32]. For brilliant green detection, the Raman shift at 1616 cm^{-1}, corresponding to the para-substituted benzene ring stretch, was utilized. Lastly, for methylene blue detection, the Raman shift at 1621 cm^{-1}, which corresponds to the C—C ring stretching band, was chosen for ***AEF*** calculation. The calculated ***AEF*** values, summarizing the enhancement achieved, are presented in Table 3. The ***AEF*** values of the Au-$Na_2Ti_3O_7$ SERS substrate for methyl red, methyl orange, brilliant green, and methylene blue are 25,800, 8000, 58,600, 68,000 for the dye concentration of 3.0×10^{-8} g/cm^2, respectively. Methylene blue on the Au-$Na_2Ti_3O_7$ SERS substrate results in the largest SERS enhancement factor for detecting the dye of 3.0×10^{-9} g/cm^2, the ***AEF*** value can achieve 185,000. The Raman signals of the dyes were clearly evident in the spectra obtained when adsorbed on Au-$Na_2Ti_3O_7$. This clearly demonstrates the remarkable capability of the Au-$Na_2Ti_3O_7$ substrate to effectively enhance the Raman signals, particularly for methylene blue detection. Regarding the mechanism of signal amplification, the enhancement observed in our study is primarily attributed to the electromagnetic enhancement, which arises from localized surface plasmon resonance generated by the self-precipitated Au nanoparticles on the titanate nanofiber surface. This conclusion is supported by TEM and XPS analyses, which confirm the presence and metallic nature of Au nanoparticles. After the dye solution was dropped onto the substrate, the dye molecules were first adsorbed and distributed along the high-surface-area fibrous network. The porous morphology enables efficient infiltration of dye molecules into the inter-fiber cavities, ensuring intimate contact with the Au nanoparticles. This close spatial proximity maximizes the interaction between the analyte molecules and the localized electromagnetic fields, thereby creating abundant hot spots and significantly amplifying the Raman response. In contrast, no significant Raman spectral shifts or new bands were observed after dye adsorption, suggesting the absence of strong chemical bonding or charge-transfer interactions. Therefore, the chemical enhancement

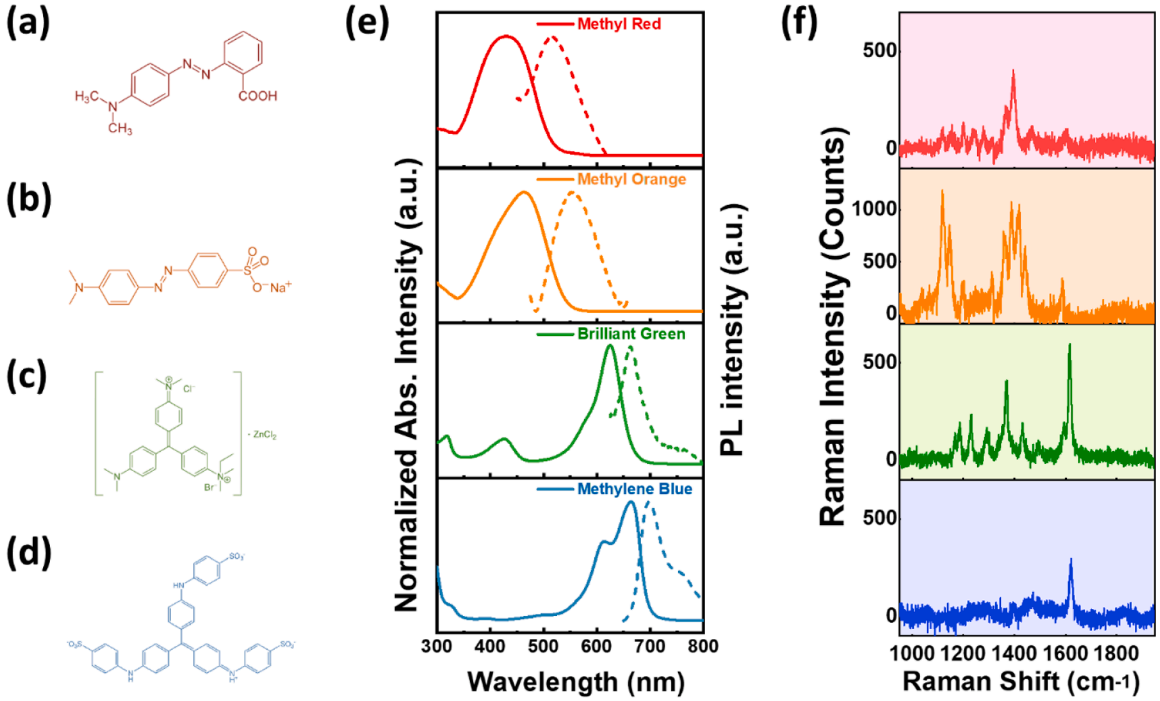

Fig. 4. Chemical structures of **(a)** methyl red, **(b)** methyl orange, **(c)** brilliant green, and **(d)** methylene blue. **(e)** UV–Vis absorption (full line) and photoluminescence spectra (dashed line) and **(f)** Raman spectra of organic dye.

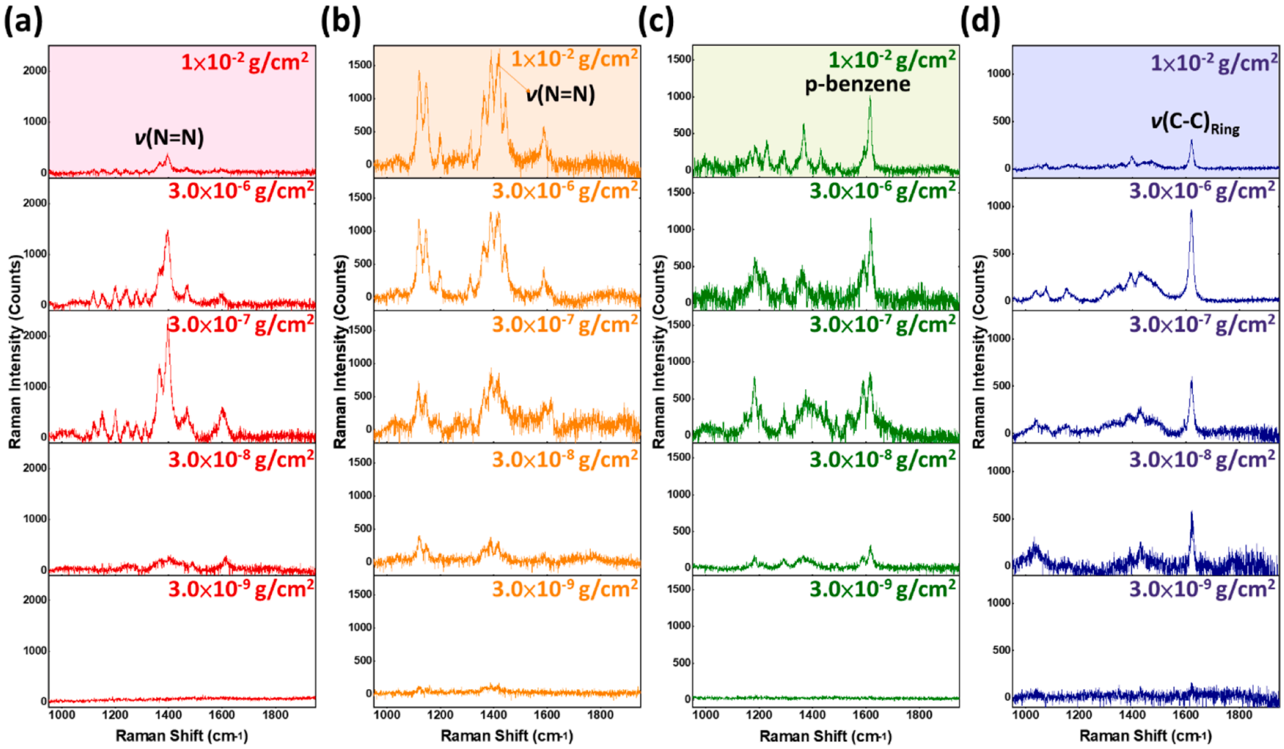

Fig. 5. Raman spectra of different concentrations of **(a)** methyl red, **(b)** methyl orange, **(c)** brilliant green, and, **(d)** methylene blue on Au-$Na_2Ti_3O_7$ nanofiber SERS substrates.

Table 3
The calculated ***AEF*** for various dye detection based on Au-$Na_2Ti_3O_7$ nanofiber SERS substrates.

Conc. (g/cm^2)	MR	MO	BG	MB
3.0×10^{-6}	1300	300	400	1100
3.0×10^{-7}	21,100	1900	3200	7000
3.0×10^{-8}	25,800	8000	58,600	68,000
3.0×10^{-9}	N.D.	35,800	N.D.	185,000

N.D.: Not detected.

mechanism is minor and negligible in this system, and the SERS activity is predominantly driven by SPR-induced electromagnetic effects.

3. Conclusion

We successfully demonstrated an easy fabricated, high sensitivity surface-enhanced Raman scattering substrates by a facial hydrothermal method to detect trace amounts of dye molecules. For Au-$Na_2Ti_3O_7$, self-precipitated Au NPs are observed on sodium titanate fibers after the hydrothermal process. The Au-$Na_2Ti_3O_7$ substrate exhibits strong adsorption capabilities and demonstrates surface plasmon resonance behavior, making it ideal for SERS applications. Through a photo-KPFM study, under green LED illumination, there is no significant difference in contact potential difference before and after illumination. This behavior allows the energy of the green laser to be primarily utilized for generating Raman scattering signals. A remarkable enhancement of 185,000-fold enhancement has been observed for methylene blue on the Au-$Na_2Ti_3O_7$ SERS substrate. This technique offers high sensitivity, low cost, and rapid response, making it suitable for the detection of organic compounds and environmental pollutant.

Disclosure use of AI-assisted technologies

During the preparation of this work the author(s) used AI-assisted technology, ChatGPT, in order to check the grammar and spell in some sentences.

CRediT authorship contribution statement

Yin-Hsuan Chang: Writing – original draft, Investigation, Formal analysis. **Ming-Chung Wu:** Writing – review & editing, Project administration, Methodology, Funding acquisition, Conceptualization. **Ting-Han Lin:** Investigation, Formal analysis. **Jia-Mao Chang:** Investigation, Formal analysis. **Yu-Ching Huang:** Writing – review & editing, Methodology. **Jer-Chyi Wang:** Writing – review & editing, Methodology.

Declaration of competing interest

The authors declare that they have no known competing financial interests or personal relationships that could have appeared to influence the work reported in this paper.

Acknowledgment

Yin-Hsuan Chang and Ming-Chung Wu contributed equally to this work. The authors appreciate Dr. Ming-Tao Lee (BL-13A1), Dr. Jeng-Lung Chen (BL-17C1) and Dr. Ting-Shan Chan (BL-01C1) at National Synchrotron Radiation Research Centre for helpful discussion and suggestions, and Mr. Y.-S. Chen at Instrumentation Centre of National Tsing Hua University for TEM analysis. The authors thank the Microscopy Center at Chang Gung University for technical assistance. The financial support from National Science and Technology Council, Taiwan (Project No. 111-2221-E-182-040-MY3, 113-2628-E-182-001-MY4, and 114-2923-E-182-001-MY3), and Chang Gung Memorial Hospital at Linkou (CMRPD2P0051, and BMRPC74) are highly appreciated. The author expresses gratitude for the financial support provided by Chang Gung University (URRPD2Q0021, URRPD2Q0031 and URRPD2Q0041).

Supplementary materials

Supplementary material associated with this article can be found, in the online version, at doi:10.1016/j.jtice.2025.106396.

References

[1] Liu C-Y, Guo J-Y, Lin J-Y, Aeimwiratchai S, Uma K, Li W-Y, et al. Significantly enhancing SERS sensitivity to distinguish pesticide concentrations at ppm levels in juices through inherent and added internal standards. J Taiwan Inst Chem Eng 2025;167:105848. https://doi.org/10.1016/j.jtice.2024.105848.

[2] Milligan K, Shand NC, Graham D, Faulds K. Detection of multiple nitroaromatic explosives via formation of a Janowsky complex and SERS. Anal Chem 2020;92(4):3253–61. https://doi.org/10.1021/acs.analchem.9b05062.

[3] Cialla-May D, Bonifacio A, Bocklitz T, Markin A, Markina N, Fornasaro S, et al. Biomedical SERS – the current state and future trends. Chem Soc Rev 2024;53(18):8957–79. https://doi.org/10.1039/D4CS00090K.

[4] Tang X, Hao Q, Hou X, Lan L, Li M, Yao L, et al. Exploring and engineering 2D transition metal dichalcogenides toward ultimate SERS performance. Adv Mater 2024;36(19):2312348. https://doi.org/10.1002/adma.202312348.

[5] Li D, Yue W, Gao P, Gong T, Wang C, Luo X. Surface-enhanced Raman spectroscopy (SERS) for the characterization of atmospheric aerosols: current status and challenges. TrAC Trends Anal Chem 2024;170:117426. https://doi.org/10.1016/j.trac.2023.117426.

[6] Yang D, Youden B, Yu N, Carrier AJ, Jiang R, Servos MR, et al. Surface-enhanced raman spectroscopy for the detection of reactive oxygen species. ACS Nano 2025;19(2):2013–28. https://doi.org/10.1021/acsnano.4c15509.

[7] Juang R-S, Wang K-S, Kuan T-Y, Chu Y-J, Jeng R-J, Hardiansyah A, et al. Electric field-stimulated Raman scattering enhancing biochips fabricated by Au nano-islands deposited on laser-scribed 3D graphene for uremic toxins detection. J Taiwan Inst Chem Eng 2024;154:105115. https://doi.org/10.1016/j.jtice.2023.105115.

[8] Sivashanmugan K, Lee H, Syu C-H, Liu BH-C, Liao J-D. Nanoplasmonic Au/Ag/Au nanorod arrays as SERS-active substrate for the detection of pesticides residue. J Taiwan Inst Chem Eng 2017;75:287–91. https://doi.org/10.1016/j.jtice.2017.03.022.

[9] Feng Z, Jia Y, Cui H. Engineering the surface roughness of the gold nanoparticles for the modulation of LSPR and SERS. J Colloid Interface Sci 2024;672:1–11. https://doi.org/10.1016/j.jcis.2024.05.217.

[10] Wang Z, Zhou Y, Wang J, Wang Y, Zhao J, Xu W, et al. Site-specific growth of Ag islands on concave Au nanocubes for SERS and LSPR-based applications. ACS Appl Nano Mater 2024;7(18):22002–10. https://doi.org/10.1021/acsanm.4c04013.

[11] Yin W, An S, Cheng T, Jiang L, Cao Y. Enhancing SERS sensitivity of semiconductors through constructing CuO@TiO2 heterojunctions via atomic layer deposition. Appl Surf Sci 2024;672:160820. https://doi.org/10.1016/j.apsusc.2024.160820.

[12] Liu W, He X, Wang Z, Yuan M, Zhao Z, Ye X, et al. Geometric and electronic structure modulation to optimize the charge transfer of TiO2 for ultrasensitive and stable SERS sensing. Inorg Chem 2024;63(38):17608–16. https://doi.org/10.1021/acs.inorgchem.4c02364.

[13] Trang TNQ, Bao NTG, Duong T, Thu VTH. Design of high-active SERS in 2D Au/TiO2 thin film for quantitative and photodegraded analysis. Chem Pap 2024;78(11):6649–61. https://doi.org/10.1007/s11696-024-03563-7.

[14] Huang Y, Zhang S, Jiang S, Xu J. Improved SERS performance on Ag-coated amorphous TiO2 random nanocavities by the enhanced light–Matter coupling effect. ACS Sustain Chem Eng 2024;12(8):3234–42. https://doi.org/10.1021/acssuschemeng.3c07472.

[15] Li Z, Han K, Zhang A, Wang T, Yan Z, Ding Z, et al. Honeycomb-like AgNPs@TiO2 array SERS sensor for the quantification of micro/nanoplastics in the environmental water samples. Talanta 2024;266:125070. https://doi.org/10.1016/j.talanta.2023.125070.

[16] Sun N, Huang B, Lv Z, Ran N, Gan Y, Zhang J. UV-catalyzed TiO2–Based optofluidic SERS chip for three online strategies: fabrication, detection, and self-cleaning. Anal Chem 2024;96(22):9104–12. https://doi.org/10.1021/acs.analchem.4c00657.

[17] Su Y, Gong M, Liu Y, Shah FU, Laaksonen A, An R. Step toward superior nanoscale biosensing: investigation of trace cytochrome c using TiO2 SERS substrates and phosphonium-based fluorine-free ionic liquid “linkers. ACS Appl Nano Mater 2025;8(12):6234–41. https://doi.org/10.1021/acsanm.5c00889.

[18] Lincho J, Mazierski P, Klimczuk T, Martins RC, Gomes J, Zaleska-Medynska A. TiO2 nanotubes modification by photodeposition with noble metals: characterization, optimization, photocatalytic activity, and by-products analysis. J Environ Chem Eng 2024;12(3):112990. https://doi.org/10.1016/j.jece.2024.112990.

[19] Kubiak A. Impact of LED radiation intensity on gold nanoparticles photodeposition on TiO2 with physicochemical and photocatalytic characterization. Sci Rep 2024;14(1):20563. https://doi.org/10.1038/s41598-024-71605-x.

[20] Lin T-H, Wu M-C, Chiang K-P, Chang Y-H, Hsu J-F, Hsu K-H, et al. Unveiling the surface precipitation effect of Ag ions in Ag-doped TiO2 nanofibers synthesized by one-step hydrothermal method for photocatalytic hydrogen production. J Taiwan Inst Chem Eng 2021;120:291–9. https://doi.org/10.1016/j.jtice.2021.03.011.

[21] Meng Z, Zhang J, Long H, García H, Zhang L, Zhu B, et al. Kelvin probe force microscopy reveals spatially resolved charge-transfer mechanism in CdS/BiOBr S-scheme heterojunction photocatalyst. Angew Chem Int Ed 2025:e202505456. https://doi.org/10.1002/anie.202505456.

[22] Moon HS, Hsiao K-C, Wu M-C, Yun Y, Hsu Y-J, Yong K. Spatial separation of cocatalysts on Z-scheme organic/inorganic heterostructure hollow spheres for enhanced photocatalytic H2 evolution and In-depth analysis of the charge-transfer mechanism. Adv Mater 2023;35(4):2200172. https://doi.org/10.1002/adma.202200172.

[23] Chang J-M, Lin T-H, Hsiao K-C, Chiang K-P, Chang Y-H, Wu M-C. Gas-solid phase reaction derived silver bismuth iodide rudorffite: structural insight and exploring photocatalytic potential of CO2 reduction. Adv Sci 2024;11(24):2309526. https://doi.org/10.1002/advs.202309526.

[24] Zeng W, Hou M, Li H, Zhong W-M, Wen S, Zhao J, et al. 2D Covalent organic framework-based heterostructure for neuromorphic visual processing. Adv Funct Mater 2025:e11687. https://doi.org/10.1002/adfm.202511687. n/a(n/a).

[25] Bie C, Meng Z, He B, Cheng B, Liu G, Zhu B. Exploring photogenerated charge carrier transfer in semiconductor/metal junctions using Kelvin probe force microscopy. J Mater Sci Technol 2024;173:11–9. https://doi.org/10.1016/j.jmst.2023.07.019.

[26] Niu X, Du Y, Liu J, Li J, Sun J, Guo Y. Facile synthesis of TiO2/MoS2 composites with Co-exposed high-energy facets for enhanced photocatalytic performance. Micromachines (Basel) 2022;13(11):1812. https://www.mdpi.com/2072-666X/13/11/1812.

[27] Amy L, Favre S, Gau DL, Faccio R. The effect of morphology on the optical and electrical properties of sodium titanate nanostructures. Appl Surf Sci 2021;555:149610. https://doi.org/10.1016/j.apsusc.2021.149610.

[28] Liu H, Yang D, Zheng Z, Ke X, Waclawik E, Zhu H, et al. A raman spectroscopic and TEM study on the structural evolution of Na2Ti3O7 during the transition to Na2Ti6O13. J Raman Spectrosc 2010;41(10):1331–7. https://doi.org/10.1002/jrs.2561.

[29] Le Ru EC, Blackie E, Meyer M, Etchegoin PG. Surface enhanced Raman scattering enhancement factors: A comprehensive study. J Phys Chem C 2007;111(37):13794–803. https://doi.org/10.1021/jp0687908.

[30] Mercedi A, Cardoni F, Toffanello F, Reguera J, Meneghetti M, Litti L. Reliable methodology for measuring SERS enhancement factor on colloidal and solid substrates: a practical guide. J Raman Spectrosc 2025;0:1–15. https://doi.org/10.1002/jrs.6776.

[31] Park S-K, Lee C, Min K-C, Lee N-S. Fourier transform Raman studies of methyl red adsorbed on γ-alumina and silica-alumina. Bull Korean Chem Soc 2004;25:1817–21.

[32] Zhang A, Fang Y. Adsorption orientations and interactions of methyl orange on negatively and positively charged colloidal silver particles. J Colloid Interface Sci 2007;305(2):270–4. https://doi.org/10.1016/j.jcis.2006.09.068.